

# PCCP

Accepted Manuscript

This article can be cited before page numbers have been issued, to do this please use: X. Li, C. Batchelor-McAuley, J. K. Noveck and R. G. Compton, *Phys. Chem. Chem. Phys.*, 2018, DOI: 10.1039/C8CP01360H.



This is an Accepted Manuscript, which has been through the Royal Society of Chemistry peer review process and has been accepted for publication.

Accepted Manuscripts are published online shortly after acceptance, before technical editing, formatting and proof reading. Using this free service, authors can make their results available to the community, in citable form, before we publish the edited article. We will replace this Accepted Manuscript with the edited and formatted Advance Article as soon as it is available.

You can find more information about Accepted Manuscripts in the [author guidelines](#).

Please note that technical editing may introduce minor changes to the text and/or graphics, which may alter content. The journal's standard [Terms & Conditions](#) and the ethical guidelines, outlined in our [author and reviewer resource centre](#), still apply. In no event shall the Royal Society of Chemistry be held responsible for any errors or omissions in this Accepted Manuscript or any consequences arising from the use of any information it contains.

# A Thermostated Cell for Electrochemistry: Minimising Natural Convection and Investigating the Role of Evaporation and Radiation

Xiuting Li<sup>+</sup>, Christopher Batchelor-McAuley<sup>+</sup>, Javor K. Novev<sup>+</sup> and Richard G. Compton\*

\* corresponding author: Richard G. Compton, Department of Chemistry, Physical & Theoretical Chemistry Laboratory, Oxford University, South Parks Road, Oxford, OX1 3QZ, United Kingdom

Email: richard.compton@chem.ox.ac.uk. Tel: +44(0)1865275 957 Fax: +44(0)1865275410

<sup>+</sup> These authors contributed equally to this work.

## Abstract

An optimised thermostated electrochemical cell is designed and implemented. This is informed by experimental and computational studies characterizing the extent to which the thermostating of an electrochemical cell via a heated bath can be realised, both with the cell closed and open to the environment. The heat transfer in the system is simulated and probed experimentally; special emphasis is put on heat loss due to radiation and evaporation. Experiments and simulations demonstrate that these two mechanisms of heat transfer lead to a steady temperature in the cell that differs from that of the thermostat by  $\sim 0.1$  K. Simulations indicate that spatial inhomogeneities in the stationary temperature drive natural convective flows with a significant velocity. These new physical insights inform the optimization of a new electrochemical cell and its application in measurements of the impact frequency of silver nanoparticles as a function of temperature.

## Introduction

Accurate kinetic measurements require precise control of the temperature. In the case of dynamic electrochemical experiments, the careful thermostating of the electrochemical cell is of paramount importance; the mass-transport, kinetics (both homogeneous and heterogeneous) and thermodynamics are all highly sensitive to temperature<sup>1-6</sup>. As a further complication, for systems studied in the absence of forced convection, the maintenance of a quiescent state needs to be ensured. This is challenging as natural convection may be driven by either thermal or concentration gradients in the cell and can lead to irreproducible flow patterns and results<sup>7,8</sup>. Even in the absence of an electrochemical reaction it is important to consider the factors that control the temperature distribution in a cell.

Over the preceding two decades there has been increased research into the study of electrochemical reactions at the nanoscale. One method of particular note and active development is the so-called nano-impact technique<sup>9-12</sup>. Here, a redox reaction is induced upon collision of a nanoparticle with a suitably potentiostated electrode, where the electrode is of microscopic dimensions and immersed into a nanoparticle suspension. The nanoparticle may either be directly oxidized/reduced or catalyse a suitable redox reaction at its surface<sup>13-20</sup>. Such experiments can yield significant information about the kinetics of the processes occurring at the nanoscale<sup>21-23</sup> beyond simply reporting the occurrence of a nano-impact event. Temperature control plays a crucial role in these nanoscale electrochemical measurements because, first, each nano-reaction will be sensitive to the local temperature environment, hence, heterogeneities in the cell's temperature need to be minimised. Second, if greater insight into the interfacial kinetics is to be gained, variable-temperature studies are highly desirable.

This work first seeks to provide model numerical and experimental results demonstrating the timescale required for a cell to reach a steady temperature when immersed into a thermostated water bath. The importance of radiation, evaporation, conduction and natural convection in controlling the heat transfer into and through the cell is exemplified by experiment and simulation. Experiments demonstrate the important physical insight that even for a 'model' system, the temperature of the cell can differ measurably from that of the heated bath used for thermostating the cell (0.05-0.2 K depending on the exact experimental details). As heat is transferred through the walls of the cell and is radiated – or transferred via evaporation in an open system – away from the top boundary, the temperature distribution even in the steady-state becomes inhomogeneous. It is shown through simulation that the influence of gravity gives rise to buoyancy flows broadly similar to those in the extensively studied Rayleigh–Bénard problem that concerns flows between horizontal solid surfaces<sup>24</sup>. Consequently, the thermostated cell tends not towards a quiescent state but a convective stationary one with a non-zero flow velocity. In the model system, only the flows generated by comparatively small temperature differences between the solution

and the thermostat ( $\sim 1$  K) are considered, as larger ones require modelling approaches whose sophistication goes beyond the aims of the present study.

With that insight into the important factors that control the thermostating of an electrochemical cell, a set of criteria for effective cell thermostating is provided and a cell is designed around it. The ability of the designed system to control the cell's temperature is demonstrated through its application to studying the oxidation of individual silver nanoparticles, evidencing the sensitivity of the reaction in terms of the frequency of events to the system's temperature. Although the chemical system upon which the cell design is validated is specific, the insights gained and design criteria outlined are of general applicability in the field of electrochemistry and beyond. An important physical insight provided by the experiments is that, unless heat transfer through evaporation and radiation is eliminated, the solution temperature approaches a steady non-homogeneous distribution which locally differs from the desired temperature by  $\sim 0.1$  K. Simulations predict that those temperature inhomogeneities sustain convective flows with velocities of  $\sim 10^{-4}$  m·s $^{-1}$ , implying that the assumption of purely diffusional mass transport needs to be critically assessed even for thermostated systems having the vertical dimensions of the ones considered here.

## Experimental

### Thermostating measurement

The model experimental system was a cylindrical container with 10 mL of deionized water, illustrated schematically in Figure 1. The inner and outer radii of the cell were  $r_{\text{in}} = 1.15$  cm and  $r_{\text{out}} = r_{\text{in}} + d_{\text{wall}}$ , where  $d_{\text{wall}} = 0.9$  mm, respectively. The cell was thermostated via a bath containing 1 L of water that was magnetically stirred and heated from below via a thermostat (Stuart Stirrer Hotplate UC 152 Ceramic plate with an SCT1 Digital Contact Thermometer). The temperature in the cell was recorded at a point situated on the cylinder axis at the vertical midpoint of the column of liquid; this was done continuously via a temperature probe (PT100 Sensor, R.S. Components Ltd, Corby, UK) over a period of  $t_{\text{exp}}$  between 560 and 600 s; the temperature of the water in the bath was measured thereafter and this value was used for  $T_{\text{thermostat}}$ . The temperature of the water in the bath was monitored and controlled continuously via a digital temperature controller (SCT1 Digital contact thermometer). The thermostating experiment in the closed cell was carried out by sealing the cell with a cap which had a hole in the middle where the probe was tightly held, while for the open-cell measurements no cap was used and the probe itself was clamped.

A control experiment was performed in a 10 mL aqueous solution containing 10 mg sodium dodecyl sulphate (SDS, Fluka). As even a small quantity of surfactant can cause the liquid surface to behave as a no-slip boundary<sup>25</sup>, this serves as a test for the appropriate interfacial hydrodynamic boundary condition. Furthermore, in order to quantify the mass flux due to evaporation, the mass of the liquid in the cell was

measured before the start of a thermostating experiment performed with it open to the environment and after its conclusion. Moreover, the mass of both a sealed and an open cell was measured continuously with an analytical balance over a 10-minute period.

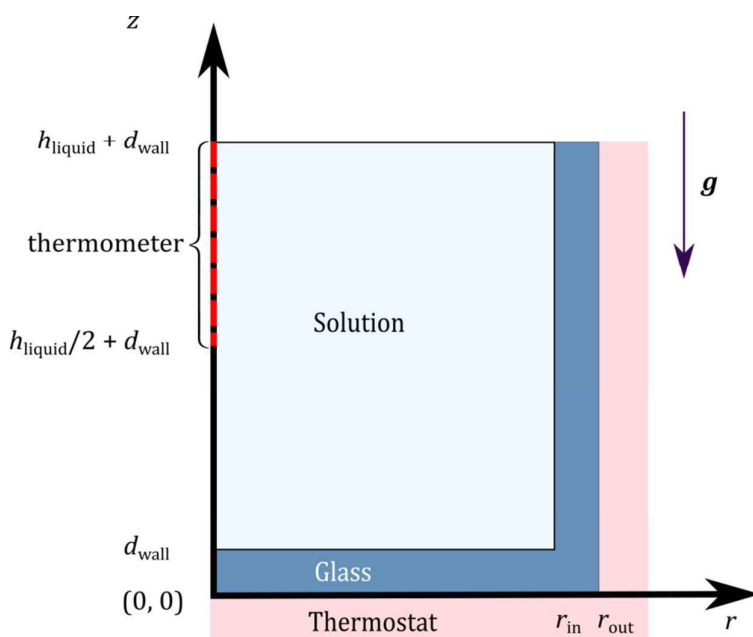
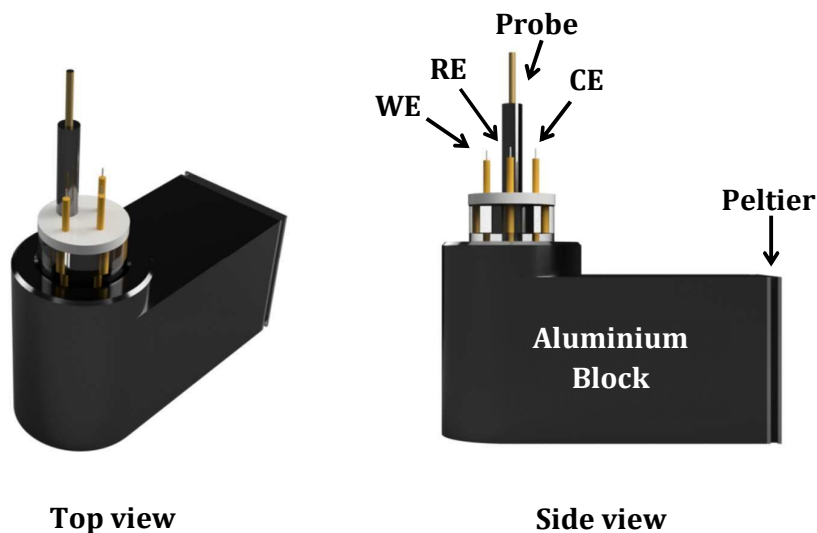


Figure 1. Sketch of the model. The solution is in a cylindrical container of wall thickness  $d_{\text{wall}}$ , inner radius  $r_{\text{in}}$  and outer radius  $r_{\text{out}}$ ; the bottom surface of the container is centred at  $(r, z) = (0, 0)$  and the solution|air interface is at  $z = h_{\text{liquid}} + d_{\text{wall}}$ . The temperature at  $(r, z) = (0, h_{\text{liquid}} + d_{\text{wall}})$  is measured via a thermometer probe.

### Design of the homemade thermostat system

The homemade thermostat system (Scheme 1) was fabricated using a Peltier-effect heat pump (type ETH-127-14-15-RS, supplied by R. S. Components Ltd, Corby, UK), 40 mm × 40 mm in area and 3.9 mm thick, with a maximum cooling capacity of 58.6 W and a maximum temperature difference of 65 K. The sample holder was an aluminium block with a cylindrical hole of diameter 22 mm and height 40 mm. A glass cell with a slightly smaller size than the hole was placed in the holder. The temperature of the solution in the glass cell was then monitored by the temperature probe (same as above) immersed in the solution. A proportional-integral-derivative (PID) loop script written in Python 3.5 controlled the Peltier element and the solution temperature. The homemade thermostat system was tested by changing and controlling the temperature of 10 mL H<sub>2</sub>O from room temperature to 25°C and 35°C. For comparison, similar experiments were also conducted with a conventional water bath-thermostat in which the cell was thermostated in a bath containing 1 L of water that was magnetically stirred and heated from below via a hotplate (Stuart Stirrer Hotplate UC152 Ceramic Plate). As described above, the temperature in the cell was continuously recorded with a temperature probe (PT100 Sensor, R.S. Components Ltd, Corby, UK), and that of the bath was monitored and controlled via a digital thermometer (SCT1 Digital contact thermometer).



Scheme 1. Schematic of the homemade thermostat system. WE, RE and CE represent the working electrode, reference electrode and counter electrode respectively. The probe together with the three electrodes is immersed in the electrochemical cell which is warmed up or cooled down by direct contact to the aluminium block controlled by a Peltier.

### Nano-impact experiments

Nano-impact experiments were performed using the homemade thermostat system as mentioned above and a home-built low-noise potentiostat which was described previously<sup>26</sup>. For the latter, a low-noise current amplifier (LCA-4K-1G, FEMTO Messtechnik GmbH, Germany) was used. The signal was digitised at 100 kS/s via a USB data acquisition device (USB-6003, National Instruments, Texas, US). Measurements were conducted on a three-electrode system in a Faraday cage. A 10  $\mu\text{m}$  diameter gold microdisc electrode (ALS, Tokyo, Japan) was used as the working electrode. A leakless Ag/AgCl (3.4 M KCl, eDAQ) and a platinum wire (Goodfellow, Cambridge, U.K.) acted as the reference electrode and the counter electrode respectively. The working electrode was polished with alumina powders from Buehler, Lake Bluff, IL, U.S.A., of decreasing sizes: 1.0, 0.3, and 0.05  $\mu\text{m}$ , followed by a thorough rinse with deionized water and drying under a nitrogen atmosphere. Cyclic voltammetric measurements initially scanning anodically in the potential range of  $E = [-0.4, 1.2]$  V vs. Ag/AgCl (3.4 M KCl) at a scan rate of 10  $\text{mV s}^{-1}$  were performed in the solutions containing 12 pM AgNPs and 20 mM KCl as supporting electrolyte. A 16-bit DAC was used to provide the waveform with a full potentiostat range of  $\pm 2$  V, effectively corresponding to staircase voltammetry with a step size of 61  $\mu\text{V}$ . Spike analysis was performed with a script written in Python.

### Theoretical Model

The thermostating of the solution occurs via heat transfer through the glass wall of the cell, and as the heat conductivity of the latter is comparable to that of the solution ( $\kappa^{\text{L}} \sim 0.6 \text{ W} \cdot \text{m}^{-1} \cdot \text{K}^{-1}$  and  $\kappa^{\text{S}} \sim 1 \text{ W} \cdot \text{m}^{-1} \cdot \text{K}^{-1}$ ), the solid phase cannot be regarded as being in

thermal equilibrium with the water bath. Thus, it is necessary to solve the heat equation for the temperature of the solid ( $T^S$ ),

$$\partial_t T^S = \chi^S \nabla^2 T^S, \quad (1)$$

where  $\chi^S$  is the thermal diffusivity of the glass.

The temperature profile in the liquid phase ( $T^L$ ) is governed by the heat equation,

$$\partial_t T^L + \mathbf{v} \cdot \nabla T^L = \chi^L \nabla^2 T^L, \quad (2)$$

where  $t$  denotes time,  $\mathbf{v}$  is the velocity of the fluid and  $\chi^L = \kappa^L / (\rho_0^L C_p^L)$  is its thermal diffusivity, with  $C_p^L$  – its specific heat capacity at constant pressure [ $\text{J} \cdot \text{kg}^{-1} \cdot \text{K}^{-1}$ ],  $\rho^L$  – the liquid density, and  $\rho_0^L$  – its value at  $T_{\text{solution } 0}$ ; below, the overall temperature distribution in the system is referred to as  $T$ . As the velocity appears in the heat equation (2), to determine the temperature, it is also necessary to solve the continuity and Navier-Stokes equations that govern the flow in the system. The following approximate form of the latter is employed:

$$\begin{aligned} \rho_0^L (\partial_t \mathbf{v} + \mathbf{v} \cdot \nabla \mathbf{v}) &= -\nabla \Delta p + \eta \nabla^2 \mathbf{v} - \rho_0^L \alpha (T^L - T_{\text{solution } 0}) \mathbf{g}, \\ \nabla \cdot \mathbf{v} &= 0; \end{aligned} \quad \begin{aligned} (3) \\ (4) \end{aligned}$$

where  $\mathbf{g}$  is the acceleration due to gravity  $\eta$  – the viscosity of the liquid,  $T_{\text{solution } 0}$  – its initial temperature,  $\alpha = -(\partial \rho^L / \partial T)_p / \rho^L$  is its coefficient of thermal expansion at  $T_{\text{solution } 0}$ ;  $\Delta p$  is the pressure difference with respect to the hydrostatic pressure in the unperturbed liquid,  $\Delta p = p - p_{\text{ref}} + \rho_0^L |\mathbf{g}| (z - h_{\text{liquid}} - d_{\text{wall}})$  with  $p_{\text{ref}}$  being a reference value, and  $z$  – the normal coordinate. Eqs. (3)-(4), adopt the Boussinesq approximation<sup>27</sup>, treating the solution density as a linear function of temperature in the buoyancy term in the Navier-Stokes equation and as constant elsewhere. Following the standard Boussinesq approach, which is valid at  $|\alpha(T^L - T_{\text{solution } 0})| \ll 1$ <sup>28</sup>, the temperature-dependence of all other properties of the liquid is neglected. Numerical solutions to equations (1)-(4) are computed via the finite-element modelling software COMSOL Multiphysics® 5.3.

The cell is treated as a perfect cylinder and it is assumed that the velocity and temperature distributions are rotationally symmetric. Accordingly, when using cylindrical coordinates,  $r$  and  $z$ , the problem only needs to be solved for the 2-dimensional region pictured in Figure 1. The coordinates are defined so that the positive  $z$  direction coincides with the symmetry axis of the cell and is aligned contrary to the gravitational acceleration  $\mathbf{g}$ , as illustrated in the figure. The geometry of the glass container in the model is chosen so that it approximately matches that of the experimental cell, having inner and outer radii  $r_{\text{in}}$  and  $r_{\text{out}} = r_{\text{in}} + d_{\text{wall}}$ . The cell contains 10 mL of water, corresponding to a fluid column of height  $h_{\text{liquid}} = 2.41$  cm. Only the heat transfer in the part of the solid cell that is in contact with the fluid, i.e.,  $z \in [0, h_{\text{liquid}} + d_{\text{wall}}]$  is considered. The temperature of the liquid is recorded at the tip of the



thermometer,  $T_{\text{probe}} = T(r = 0, z = h_{\text{liquid}}/2 + d_{\text{wall}})$ ; in the present model, the latter is an infinitesimally thin line at  $r = 0$  and  $z \in [h_{\text{liquid}}/2 + d_{\text{wall}}, h_{\text{liquid}} + d_{\text{wall}}]$ .

Initially, the temperature within the solution and the glass container is homogeneous and differs by  $\Delta T = T_{\text{thermostat}} - T_{\text{solution } 0} \sim 2$  K from that of the thermostat. It is assumed that the temperature of the stirred water bath is homogeneous and fixed at  $T_{\text{thermostat}} = 298.15$  K throughout the experiment. Thus, at all times, the temperature of the outside walls of the container is

$$T^S|_{r \in [0, r_{\text{out}}], z=0} = T^S|_{r=r_{\text{out}}, z \in [0, h_{\text{liquid}}+d_{\text{wall}}]} = T_{\text{thermostat}}. \quad (5)$$

Three types of boundary conditions for the top boundary of the cell are used. The first one corresponds to the limiting case in which the cell is thermally insulated and there is no normal heat flux through the surface  $z = h_{\text{liquid}} + d_{\text{wall}}$ ,

$$\kappa^L \partial_z T^L|_{r \in [0, r_{\text{in}}], z=h_{\text{liquid}}+d_{\text{wall}}} = 0 \text{ and} \quad (6)$$

$$\kappa^S \partial_z T^S|_{r \in [r_{\text{in}}, r_{\text{out}}], z=h_{\text{liquid}}+d_{\text{wall}}} = 0. \quad (7)$$

As the top of the experimental cell is not in fact thermally insulated, a more realistic boundary condition for  $z = h_{\text{liquid}} + d_{\text{wall}}$  has to consider the heat transfer with the environment. Here, it is assumed that eq. (7) remains valid, but the liquid loses heat via grey-body radiation, corresponding to a heat flux of

$$\kappa^L \partial_z T^L|_{r \in [0, r_{\text{in}}], z=h_{\text{liquid}}+d_{\text{wall}}} = -\varepsilon \sigma (T^4 - T_{\text{ambient}}^4)|_{r \in [0, r_{\text{in}}], z=h_{\text{liquid}}+d_{\text{wall}}}, \quad (8)$$

where  $\varepsilon = 0.96$  is the emissivity of pure water<sup>29</sup>,  $\sigma = 5.67 \times 10^{-8} \text{ W} \cdot \text{m}^{-2} \cdot \text{K}^{-4}$  is the Stefan-Boltzmann constant, and  $T_{\text{ambient}} = 296.15$  K is the temperature of the air in the laboratory. If the liquid is close to thermal equilibrium with the thermostat, eq. (8) gives an outward flux of approximately  $11.4 \text{ W} \cdot \text{m}^{-2}$ . Strictly viewed, eq. (8) is a gross approximation as it is only valid for heat transfer to an infinite medium whose temperature is homogeneous and equal to  $T_{\text{ambient}}$ . In the real system, if the cell is sealed, the liquid is in direct contact with only a small volume of air that is separated from the outer environment by the cap. Furthermore, there are contributions to heat transfer not just from radiation but also from convection in the gas; however, as shown below, this treatment leads to satisfactory agreement with the experimental data.

Lastly, when simulating experiments in which the cell is open to the environment and evaporation takes place, it is necessary to account for the heat loss due to evaporation. Weighing the system before and after the experiment indicates that conducting the experiments with a cell open to the environment results in a mass loss  $\Delta m$  of approximately 4 mg, in contrast with the case of a sealed cell, whose mass remains constant within 0.1 mg. The mass loss due to evaporation in an open cell corresponds to a considerable heat flux from the cell to the environment – the heat loss is  $\Delta H = \Delta H_e^L \Delta m$ , where  $\Delta H_e^L(T = 298.15 \text{ K}) = 2.44 \text{ kJ} \cdot \text{g}^{-1}$  is the vaporization enthalpy of water<sup>30</sup>. The temperature of the liquid would change by approximately  $\Delta T_{\text{evaporation}} = \Delta H / (V \rho_0^L C_p^L) \approx 0.2$  K (where  $V$  is its volume), if it lost the same amount



of heat via a quasi-static process in the absence of thermostating. This considerable outward heat flux can be expected to have a strong effect on the temperature distribution in the cell, and is included in the model by imposing a constant heat flux at the surface,

$$\kappa^L \partial_z T^L|_{r \in [0, r_{\text{in}}], z = h_{\text{liquid}} + d_{\text{wall}}} = -\frac{\Delta H_e^L \Delta m}{\pi r_{\text{in}}^2 t_{\text{exp}}} \approx -39.2 \text{ W} \cdot \text{m}^{-2}. \quad (9)$$

Eq. (9) is an approximate value of the heat flux averaged over the area of the interface and the duration of the experiment; thus, it ensures that the total amount of heat transferred due to evaporation in the model and the experiments is identical. A more detailed account of evaporative heat flux would require modelling additional effects, such as the mass transport of vapour in the air surrounding the cell and would thus go outside the scope of the current study. Furthermore, the use of a condition for constant flux is indirectly supported by measurements of the mass of an open cell as a function of time - in these experiments, the total mass of the liquid  $m$  decreases approximately linearly with  $t$ . However, it should be noted that the  $m(t)$  measurements are conducted under conditions different from those for the thermostating experiments, which may affect the evaporative flux.

At the solid-liquid boundaries, the temperature and the conductive heat flux are continuous; the assumed symmetry of the system dictates that the radial flux is equal to zero at  $r = 0$ . These conditions are handled by the COMSOL Multiphysics® *Heat Transfer in Fluids* module, which utilizes quadratic elements for the temperature distributions  $T^L$  and  $T^S$ .

For the hydrodynamic problem, it is assumed that initially, the fluid is at rest and  $\Delta p = 0$  throughout it. At the liquid|solid interfaces, including the thermometer probe, no-slip boundary conditions are imposed at all times,

$$\begin{aligned} \mathbf{v}|_{r=0, z \in [h_{\text{liquid}}/2 + d_{\text{wall}}, h_{\text{liquid}} + d_{\text{wall}}]} &= \mathbf{v}|_{r=r_{\text{in}}, z \in [d_{\text{wall}}, h_{\text{liquid}} + d_{\text{wall}}]} = \\ \mathbf{v}|_{r \in [0, r_{\text{in}}], z = d_{\text{wall}}} &= \mathbf{0}. \end{aligned} \quad (10)$$

Furthermore, it is assumed that the velocity in the fluid is not affected by mass transport through the surface  $z = h_{\text{liquid}} + d_{\text{wall}}$ ; therefore,  $v_z$  is restricted to 0 there. Similarly to the heat transport problem, symmetry imposes a condition, at  $r = 0$ , in this case,  $v_r = 0$ ; analogously, this condition is built-in in the COMSOL Multiphysics® *Laminar Flow* module. Quadratic elements are used for the velocity components and linear ones for the pressure (P2 + P1) in the hydrodynamic problem. Since the fluid is assumed incompressible, only the gradient of the pressure is physically meaningful<sup>31</sup>. To ease the numerical solution of the problem,  $\Delta p$  is offset by a function of time through imposing the constraint  $\Delta p(r = r_{\text{out}}, z = h_{\text{liquid}} + d_{\text{wall}}) = 0$ .

The stress balance at the liquid|gas interface is discussed next. Curvature effects are neglected at the interface, and the latter is treated as planar; as the shape of the surface is prescribed in advance, it is not possible to impose a local balance of stress in

the normal direction<sup>32</sup>. As for the surface tangential stress, here it is modelled via two types of boundary conditions for the velocity profile at the liquid|gas interface. The first of these is a constraint known as a free-surface boundary condition<sup>7</sup>, which is a form of tangential mass balance at the interface that neglects the viscous stresses in the gas phase on account of it having a much lower velocity than the liquid, leading to the form

$$\eta(\partial_r v_z + \partial_z v_r)|_{r \in [0, r_{in}], z = h_{liquid} + d_{wall}} = 0, \quad (11)$$

where it follows from the condition imposed on  $v_z$  at the interface that the first term in parenthesis is identically zero. Here, the spatial variation of the surface tension with temperature and the resulting Marangoni flows are neglected – see SI Section 1 for a brief justification.

Due to the ubiquity of surface-active contaminants, in many cases liquid surfaces behave as no-slip boundaries instead of free ones, see Refs. <sup>25</sup> and <sup>33</sup>. For this reason, the contrasting limiting case of a no-slip boundary is also considered,

$$v|_{r \in [0, r_{in}], z = h_{liquid} + d_{wall}} = 0. \quad (12)$$

Note that even at the small  $\Delta T$  considered here, the experimental system is strongly driven, with Rayleigh numbers  $Ra$  ranging from  $3.3 \times 10^5$  to  $5.4 \times 10^5$  in the experimentally studied interval for  $\Delta T$  ([1.3, 2.3] K, see SI Section 1 for information on how  $Ra$  is calculated). Thus, the flows may no longer fulfil the assumption for axial symmetry upon which the model is based – see e.g. Ref. <sup>34</sup>, where the transition to 3-D flows in a cylinder with a partially heated lateral walls and cooled horizontal walls is studied. However, the approximate treatment as outlined above fulfils the study's aims for semi-quantitative agreement between simulation and experiment.

A useful characteristic of a convective flow is the magnitude of its velocity averaged over the whole volume of the liquid  $V$  as per the equation

$$|v_{av}| = \frac{1}{V} \int_V \sqrt{v_r^2 + v_z^2} dV. \quad (13)$$

## Results

The following section considers the thermostating of an electrochemical cell with a water bath, first with the cell sealed and then with it open to the environment. Insights into the system's heat transfer are gained through numerical simulation and model experiments. Observations from both dictate a set of design criteria, and a thermostating system that fulfils them is developed. The application of this thermostat is evidenced and validated through a preliminary study on the influence of the experimental temperature upon the oxidation of individual silver nanoparticles.

## Thermostating a Closed Cell

A glass vial containing 10 mL of de-ionised water was immersed into a water bath set at 298.15 K; the temperature of the liquid in the vial was initially lower than that of the heated bath by 1.3 K. The vial was sealed with a cap and the temperature of the liquid inside it monitored as a function of time. The results for the difference between the temperature of the thermostated water bath and that of the probe ( $\Delta T_{\text{probe}}$ ) are plotted in Figure 2; two key observations can be made from this plot. First, it takes approximately 300 seconds for the probe to reach within a temperature 0.1 K of that of the bath. Second, even for this closed cell, the temperature of the water inside the vial does not become equal to that of the water bath even after thermostating for  $t_{\text{exp}} = 600$  s – the temperature of the water in the vial stabilises to approximately 0.1 K below that of the water bath. This difference between the temperatures of the two environments was confirmed by transferring the temperature probe into the water bath at the end of the thermostating experiment, ensuring the discrepancy is not simply associated with the accuracy of the thermometer. Importantly, the magnitude of this discrepancy between the temperatures of the two environments at steady state is sensitive to the vertical position of the vial within the water bath. As shown in the SI (Section 6), immersion of the cell further into the water bath enables the temperature difference to be decreased to a magnitude of ca. 50 mK, but not fully eliminated. This sensitivity to the used cell depth demonstrates that the temperature of the glass vial above the internal water line can have a non-negligible and measurable influence on the temperature control of a sample; it also suggests that, contrary to the assumption of the present model, the temperature distribution in the water bath is not homogeneous. However, this is not considered in the current semi-quantitative treatment of the problem.

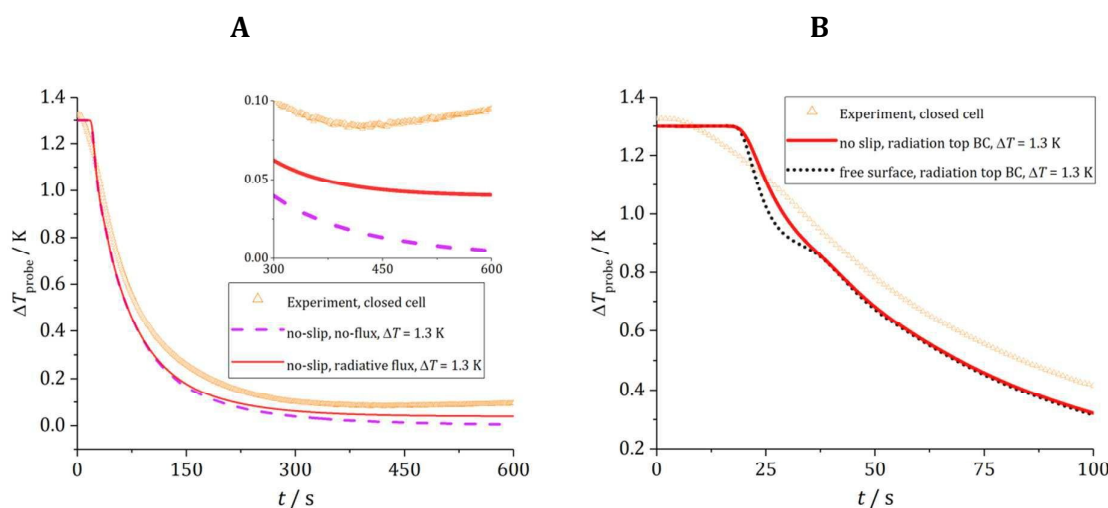


Figure 2. Difference between the temperature of the thermostat and that at the measurement point ( $\Delta T_{\text{probe}}$ ) as a function of time at an initial  $\Delta T$  of 1.3 K. A. Comparison of experimental data (points) and simulations with a no-slip boundary having 1) a no-flux boundary condition (dashed line) and 2) a radiative heat flux condition at the liquid|air interface (solid line). Note that the simulation with boundary condition for thermal insulation predicts that the solution temperature asymptotically tends towards  $T_{\text{thermostat}}$ , whereas the one with radiative heat flux predicts a

temperature difference close to the experimentally observed one. **B.** Plot of the experimental data from **A** at short times and calculated values for simulations with radiative heat flux, 1) a no-slip hydrodynamic boundary condition (solid line) and 2) a free-surface one (dashed line). The free-surface simulation predicts fluctuations in  $\Delta T_{\text{probe}}$  that are not observed experimentally; both curves go through several inflections (see text), although this is not clearly visible at this scale for the one with a no-slip boundary condition. Note that the choice of boundary condition for the hydrodynamic problem has only a minor effect on the measured temperature and that its influence is insignificant beyond  $t \approx 50$  s; the comparison with experimental data suggests that a no-slip condition is more appropriate.

The experimental data in Figure 2 is overlaid with results from simulations performed with a no-slip hydrodynamic boundary condition. The model correctly predicts the time scale for approaching a thermal steady state and satisfactory agreement is observed between the experimental and simulated curves.

The model accounts for the conduction of heat across the glass walls of the cell and convective heat transfer in the internal aqueous environment, whereas the temperature of the water bath is taken to be homogeneous and independent of time. If a condition for zero heat flux is imposed at the liquid|gas interface, the temperature of the cell is predicted to asymptotically approach the temperature of the heated bath. If instead the radiative heat flux condition (8) is assumed at the interface, the balance between heat lost to radiation and gained from the water bath leads to a predicted temperature difference of  $\approx 0.04$  K at  $t = t_{\text{exp}}$ . This value is in excellent agreement with the one measured experimentally for a cell deeply immersed (SI Section 6) into the water bath and demonstrates that even for a closed cell system imperfections in the thermostat and radiative heat flux can lead to a measurable difference in the temperature between the cell and the water bath.

The correspondence between the simulated and experimental results suggests that the present model correctly accounts for the main factors at play. Consequently, some of the features of the flow and heat transfer are considered below for the simulations with radiative heat flux and a no-slip boundary condition at the liquid|gas interface as illustrated in Figure 2. The primary observation is that the rate at which the cell approaches a steady temperature distribution is chiefly determined by the thermal convective flows thermostating induces in the cell. If a simulation is conducted at  $\Delta T = 1.3$  K with a radiative flux boundary condition at the liquid|gas interface and convective heat transfer is neglected completely,  $\Delta T_{\text{probe}}$  diminishes to within 0.1 K over a time scale of approximately 475 s, in sharp contrast with the  $\approx 213$  s predicted by the simulation of the same case that includes natural convection and a no-slip boundary condition.

The simulated curve in Figure 2, corresponding to  $\Delta T = 1.3$  K and radiative heat transfer, has a shallow maximum at short times ( $t \approx 15.5$  s) – this is due to the heat loss through radiation – for this particular initial condition, the solution is warmer than the air at  $t = 0$  and loses heat to it in accordance with eq. (8). However, the magnitude of the maximum in question ( $T - T_{\text{solution } 0} \sim 5 \times 10^{-5}$  K) is well below the accuracy of the experimental data and is therefore disregarded. More importantly, the curve goes through four inflections in the interval  $t \in [15 \text{ s}, 45 \text{ s}]$  that are not observed experimentally. These inflections are much more pronounced for the simulation with

free-surface boundary condition, as illustrated in Figure 2B, and are not seen in the experimental data, suggesting that the no-slip boundary condition is the more adequate one for the problem under study. As the curvature of the line in that region is close to zero, the inflections in question are not easily visible even in Figure 2B, which zooms into the region of short times. As discussed above, a no-slip boundary condition is appropriate for experiments conducted in the presence of a surfactant; the fact that no qualitative difference in  $\Delta T_{\text{probe}}$  is seen when the measurements are performed in that way is additional evidence that even the surface of distilled water behaves as a no-slip boundary.

The reason for the predicted disturbances in  $\Delta T_{\text{probe}}$  is that the flow field undergoes complex evolution during that period. Figure 3 shows the distributions of  $T$  and  $\mathbf{v}$  together with the streamlines of the flow. After an induction period in which convection does not affect the heat flow significantly (Figure 3A), the heating from the sides and the bottom generates a convective cell with anticlockwise motion in the studied region. This circulatory flow carries a warm front at the upper part of the cell radially inward towards the cylinder axis and downwards (Figure 3B). At  $t \sim 30$  s, the system transitions from a regime with a single convective cell occupying the simulated region to one with a secondary counterrotating cell in the vicinity of the cylinder axis (compare Figure 3 B and C). The presence of the latter cell distorts the streamlines of the flow and thus also the heat transfer at  $r \sim 0$ , thus perturbing the temperature at the probe. At long times ( $t \gtrsim 120$  s), the warm fronts carried by the two convective cells meet and after their merging, the cell is again occupied by a single convective roll with anticlockwise motion in the studied region. A qualitatively similar transient flow field has been observed in Ref. <sup>35</sup>, where the case of a cylinder with heated side walls, a cooled top wall and an insulated bottom wall was considered, with the difference that in the system studied here, the extent of the secondary flow is limited by the presence of the thermometer probe. The disturbances in  $\Delta T_{\text{probe}}$  generated by these changes in the flow are more significant for the free-surface system as the average flow velocity in the solution is higher in this case (see Figure S8 in SI7), causing the temperature to be more strongly perturbed by the development of the velocity distribution than for a no-slip surface, as Figure 2B illustrates. A simple analysis given in the SI (Section 3) indicates that perturbations such as those for the free-surface case could be recorded by our experimental equipment if they arose in the real system. As this is not the case, only results obtained with a no-slip surface condition are discussed hereafter. It should be borne in mind, though, that  $\Delta T_{\text{probe}}$  in the present model may be more prone to disturbances than in reality, as the measured temperature is averaged over an area rather than recorded at a single point.



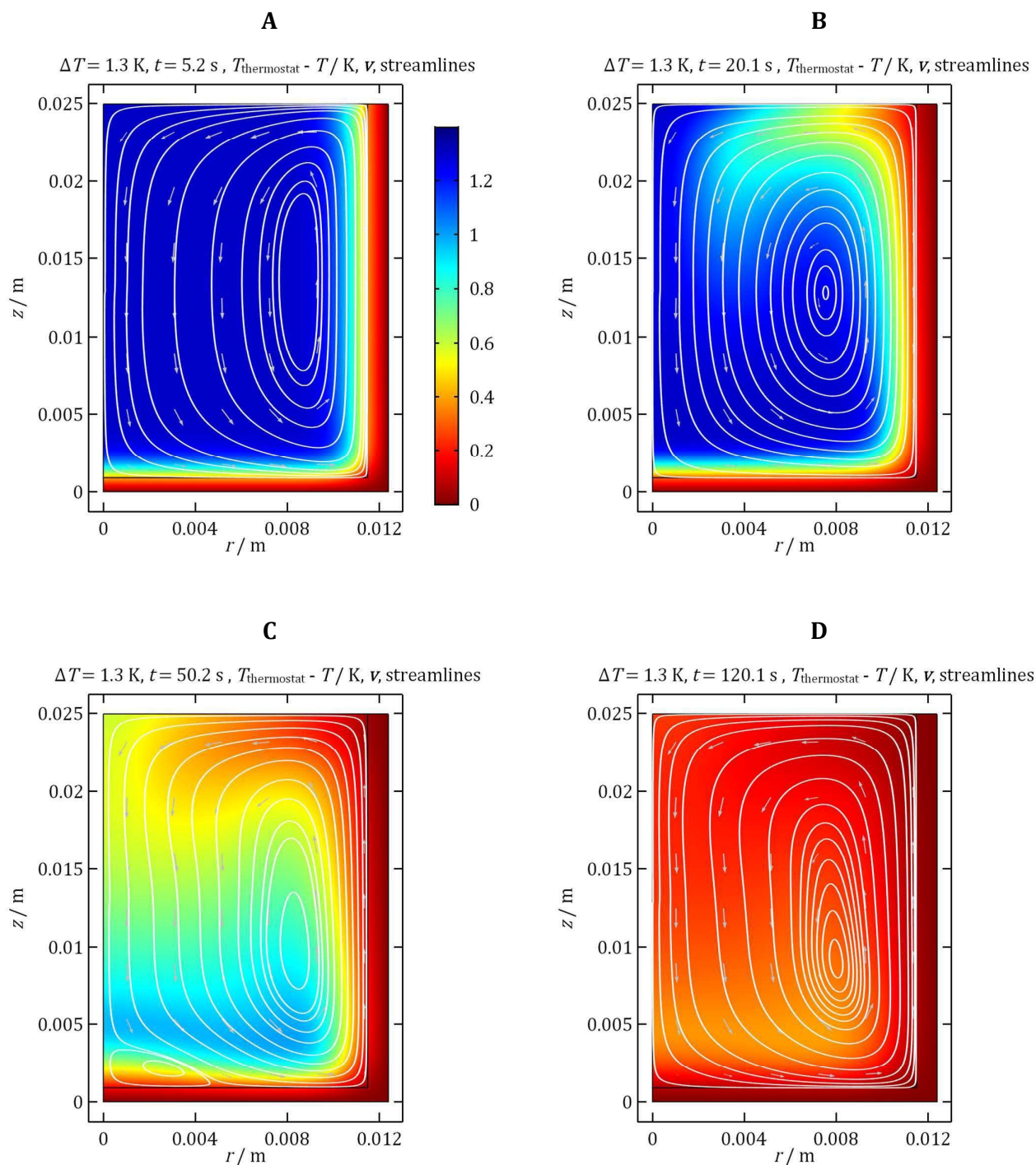


Figure 3. Temperature distribution, streamlines and arrow plot of the velocity field for a simulation with a no-slip surface, a boundary condition for radiative heat transfer through the liquid|gas interface and  $\Delta T = 1.3$  K. In each plot, the length of the arrows is proportional to the local value of  $|\mathbf{v}|$ , but the proportionality constant varies between frames. Note the evolution of the flow pattern and the direction of the main flow, which is dictated by the heating at the cell wall  $r = r_{\text{out}}$ . Heat exchange causes the fluid density to become lower in the vicinity of the inner cell wall, leading to a positive local  $v_z$  and an anticlockwise flow in the shown region.

Notably, even for this closed-cell system the radiative flux of heat from the top surface provides a driving force for convection at all times and the system tends towards a stationary state with a non-zero velocity field and a spatially inhomogeneous



temperature. Furthermore, the cooling of the upper layer of liquid due to the radiative flux leads to a configuration unstable with respect to convection and sustains circulation throughout the whole cell. Thus, regardless of the initial temperature difference, the system tends to a convective stationary state and at  $t = 600$  s, the simulations predict local differences  $T^L - T_{\text{thermostat}}$  of up to  $\sim 0.1$  K and a single roll that occupies the whole cell and has a maximum local velocity of  $\sim 3 \times 10^{-4} \text{ m} \cdot \text{s}^{-1}$ . The local temperature difference is largest in the vicinity of the point  $(r, z) = (0, d_{\text{wall}} + h_{\text{liquid}})$ , and the velocity is maximal in the vicinity of the temperature probe  $(r, z) = (0, d_{\text{wall}} + h_{\text{liquid}}/2)$ .

Increasing the initial temperature difference  $\Delta T$  qualitatively changes the observed flow patterns and thus also affects the simulated  $\Delta T_{\text{probe}}$ . At  $\Delta T = 1.8$  K, the secondary convective cell at  $r = 0$  and  $z \sim d_{\text{wall}}$  becomes more distorted along the  $z$ -axis, forming an elongated roll. This secondary roll carries warm fluid from the heated wall surface to a considerably greater height than at  $\Delta T = 1.3$  K and thus perturbs the temperature distribution more strongly (see Figure S.5 in the SI), leading to greater changes in the curvature of  $\Delta T_{\text{probe}}(t)$  and three inflections. As at  $\Delta T = 1.3$  K, at long times ( $t \sim 150$  s), the flow reverts to a single convective cell through the merging of the main and secondary rolls, the difference being that the velocity in the secondary cell exceeds that in the main one at intermediate timescales, explaining the stronger effect on  $\Delta T_{\text{probe}}$ . A comparison of the simulated and measured  $\Delta T_{\text{probe}}(t)$  at  $\Delta T = 1.8$  K, as well as additional data on the distributions of  $T$  and  $\mathbf{v}$  at  $\Delta T = 1.3$  and  $1.8$  K, including animations of their evolution, is available in the Supplementary Information.

### Thermostating an Open Cell

After highlighting the complexities in thermostating a closed-cell system, the situation in which the cell is open to the environment is considered. Data for  $\Delta T_{\text{probe}}$  from two such experiments at  $\Delta T = 2.3$  K where the cell has not been sealed are shown in Figure 4. As before, the cell approaches a stationary temperature over a time frame of approximately 600 s. However, the major difference is that at long times the measured temperature is notably less stable and the temperature difference between the cell and the water bath is now  $\sim 0.2$  K. This increased value of  $\Delta T_{\text{probe}}$  reflects the influence of evaporation upon the system.

Figure 4 compares the predicted  $\Delta T_{\text{probe}}$  for two simulations - one that only takes radiative heat transfer through eq. (8) and one that combines it with the approximate account for the effect of evaporation on temperature through the constant-flux boundary condition (9). The combination of eqs. (8) and (9) predicts  $\Delta T_{\text{probe}}(t_{\text{exp}}) \approx 0.15$  K, comparing better with the experiment than the value  $\Delta T_{\text{probe}}(t_{\text{exp}}) \approx 0.04$  K resulting from eq. (8) alone. It should be noted that simulations utilizing the evaporative heat flux boundary condition (9) predict that  $\Delta T_{\text{probe}}$  initially exhibits an increase and goes through a maximum of height  $T(t \approx 15 \text{ s}) - T_{\text{solution } 0} \sim 0.01$  K. This is due to the cooling effect of evaporation which is felt at the probe before the heating from the thermostat. However, the existence of this maximum cannot be ascertained with the

experimental data in this study - in the initial period, the temperature recorded by the probe exhibits large fluctuations because it is briefly exposed to the air as the cell is immersed in the bath.

The cooling of the upper layers of the cell via radiation at long times is in this case reinforced by the evaporative heat loss and the combination of them leads to sustained convective currents of greater intensity than in the case of a cell sealed to the environment. The simulations performed as part of this study predict local differences in the temperature of the cell up to  $T_{\text{thermostat}} - T^L = 0.3$  K and maximum local velocity magnitudes of the convective flows of  $\approx 8 \times 10^{-4} \text{ m} \cdot \text{s}^{-1}$ . As in the case with no evaporation (see above), the flow at  $t = t_{\text{exp}}$  is a single roll and its maximum velocity is in the region of the temperature probe  $(r, z) = (0, d_{\text{wall}} + h_{\text{liquid}}/2)$ , with the largest temperature difference in the region of the point  $(r, z) = (0, d_{\text{wall}} + h_{\text{liquid}})$ . Consequently, experiments conducted in cells open to the environment are even more susceptible to convective effects. It should also be noted that evaporation can be expected to be of even higher importance for systems in which, in contrast to the present case, surface effects dominate over bulk ones, for example thin liquid layers.

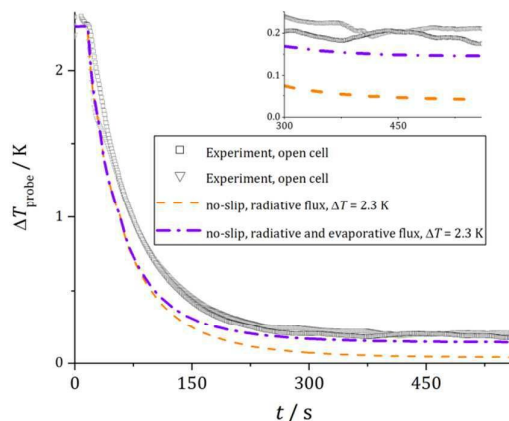


Figure 4. Difference between the temperature of the thermostat and that at the measurement point ( $\Delta T_{\text{probe}}$ ) as a function of time at initial  $\Delta T$  of 2.3 K. The two sets of points correspond to experimental measurements for a cell open to the environment. Points at short  $t$  are not shown as they deviate strongly from the trend because when the cell is placed in the water bath, the thermometer probe is exposed to the air. The curves represent simulations with a no-slip surface and different thermal boundary conditions at the liquid|gas interface: 1) radiative heat flux (dashed line) and 2) radiation and evaporative heat flux (dash-dot line). The simulation that includes both evaporative and radiative heat transfer is in closer agreement with the experimental data, suggesting that the model including these two mechanisms for heat exchange is the most adequate for an open cell.

### Thermostating Insights and Design Criteria

Several important insights can be extracted from the model experiments on thermostating both an open and a closed-cell system and from the simulations of them. First, the simulations described here indicate that even a cell in contact with an ideal thermostat would not reach its exact desired temperature at the stationary state unless heat losses due to radiation and evaporation are eliminated. Hence, accurate reporting

of a cell's temperature requires measurements to be made in the cell and not at the thermostat. Second, these temperature differences arise from cooling of the upper layers of solution by radiative and/or evaporative mechanisms leading in all cases to the system tending towards a convective stationary state. These convective flows can be non-negligible, having a volume-average velocity  $|\mathbf{v}_{av}|$  of ca.  $10^{-4} \text{ m}\cdot\text{s}^{-1}$  for the present system. At the end of simulated experiment,  $t = t_{exp}$ ,  $|\mathbf{v}_{av}|$  has the value  $\sim 1 \times 10^{-4}$  for a closed cell – simulations with initial temperature differences  $\Delta T = 1.3$  and  $1.8 \text{ K}$  respectively yield  $\approx 6.5 \times 10^{-5}$  and  $\approx 6.6 \times 10^{-5} \text{ m}\cdot\text{s}^{-1}$ ; the reason the initial condition has an influence on the final value of  $|\mathbf{v}_{av}|$  is probably that a true steady state is not yet reached at  $t = t_{exp}$ . For an open cell, simulations accounting for evaporation at  $\Delta T = 2.3 \text{ K}$  predict that  $|\mathbf{v}_{av}|$  reaches  $\approx 1.7 \times 10^{-4} \text{ m}\cdot\text{s}^{-1}$  and  $\approx 1.5 \times 10^{-4} \text{ m}\cdot\text{s}^{-1}$  with and without radiative heat transport, respectively – see SI Section 7 for more details. Thus, the minimisation of evaporation by using a closed cell system is essential. Third, the rate at which the system tends towards a steady state is mainly dictated by the convective heat transfer within it. Maintenance of a thermostated system will preferentially use forced convection between experiments to increase the rate of heat transfer and lead to an approximately homogeneous cell temperature.

A thermostating system was built on the basis of the above three design criteria. An additional desirable feature of the system was to be able to both raise and lower the temperature of the cell relative to the ambient conditions. The design of the thermostat system is described in the experimental section and a schematic of it shown in Scheme 1. In this system, the probe together with the three electrodes is immersed in the cell directly, and the latter is sealed with a cap. During the course of the temperature control, a flow of nitrogen is used to simultaneously degas the solution and provide forced convection, ensuring an approximately homogeneous temperature distribution in the cell. SI Section 8 presents data showing the variation of the cell's temperature as a function of time, evidencing that the thermostating of the cell is achieved within 600 s. Comparison is made to a cell which has been placed in a pre-thermostated water bath.

### Variable temperature study of AgNPs Nano-Impacts

Nano-impacts of AgNPs were investigated at different temperatures by using cyclic voltammetry. Measurements were performed by initially scanning anodically in the potential range of  $-0.4 \text{ V}$  to  $1.2 \text{ V}$  vs. Ag/AgCl (3.4 M KCl) in 12 pM AgNPs suspensions containing 20 mM KCl at a gold microdisc electrode (10  $\mu\text{m}$  in diameter) with a scan rate of 10 mV/s. Figure 6 shows representative cyclic voltammograms exhibiting nano-impact spikes of AgNPs oxidation at 35°C, 25°C, 15°C and 5°C respectively. These peaks in the current  $I$  correspond to the arrival of individual nanoparticles at the electrochemical interface and their subsequent oxidation. Spike analysis shows that the magnitude of the spike charge is similar at all temperatures (around 0.3 pC) and consistent with the oxidation of a single 50nm AgNPs after correction for irregularities in nanoparticle shape.<sup>23</sup> However, as can be seen in Figure 6 is that the height (peak current) of the spikes is highly sensitive to the system's

temperature. The height of the spike reflects the *rate* of the nano-electrochemical oxidation and it is shown to increase with temperature from 5°C to 35°C.

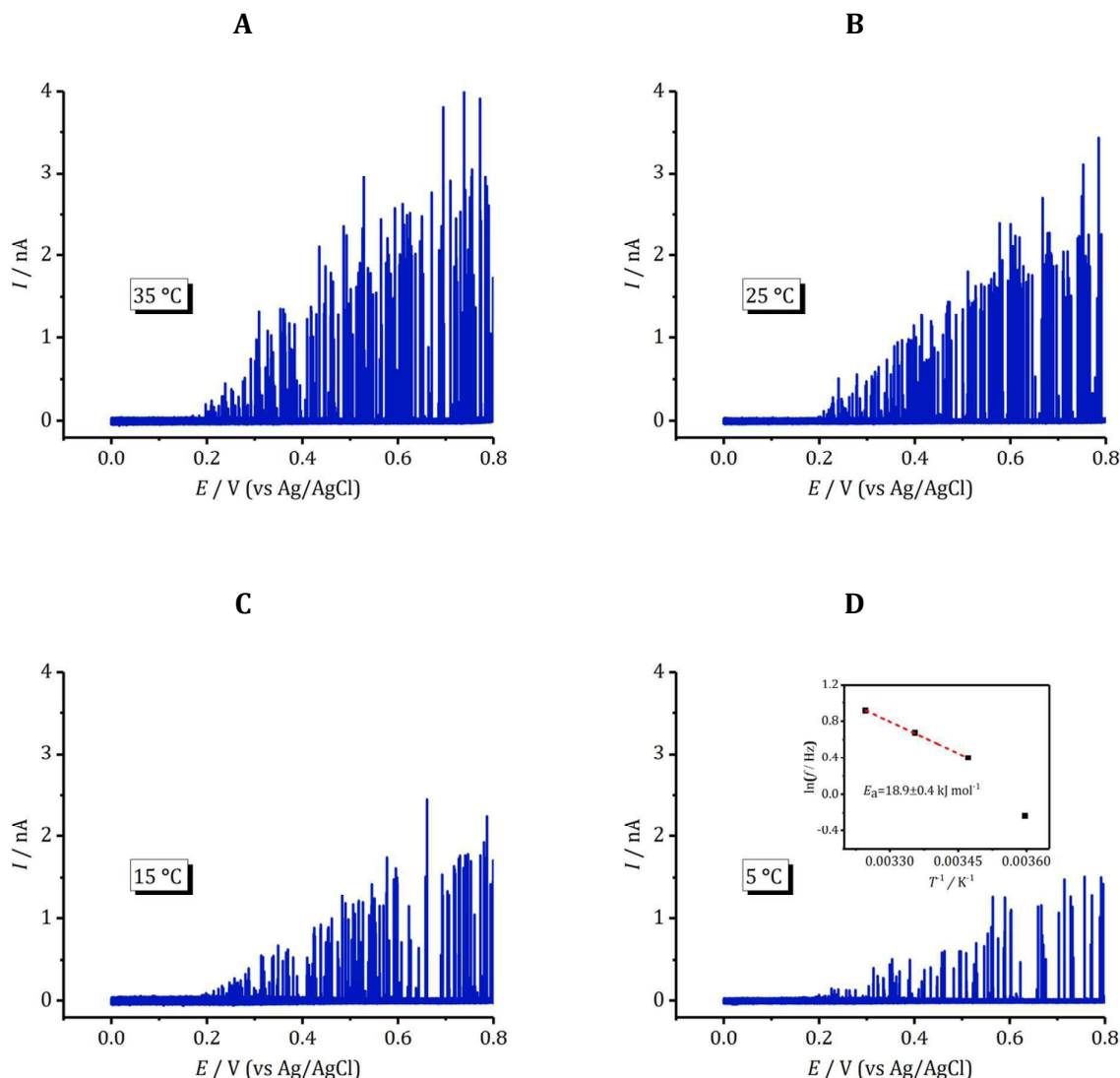


Figure 5. Representative cyclic voltammograms showing nano-impact spikes of 12 pM AgNPs in 20 mM KCl at 35°C (A), 25°C (B), 15°C (C) and 5°C (D). Gold microelectrode (10  $\mu\text{m}$  diameter) as working electrode. Scan rate: 0.01 V/s. The inset shows the variation of the collision frequency as a function of temperature.

The spike frequency was determined by dividing the number of spikes collected in the potential range of 0.2–0.8 V (vs. Ag/AgCl) on the forward scan by the period of measurement (60 s per scan). In the experiments, 895 spikes, 470 spikes, 446 spikes and 238 spikes were recorded in total on 6 scans (360 s) at 35°C, 4 scans (240 s) at 25°C, 5 scans (300 s) at 15°C and 5 scans (300 s) at 5°C. Thus, the average frequency is calculated to be 2.5, 2.0, 1.5 and 0.8 Hz at 35°C, 25°C, 15°C and 5°C respectively, demonstrating the high sensitivity of the spike frequency to the temperature. The inset of Figure 5C depicts an Arrhenius plot for the variation of the impact frequency as a

function of the temperature. For the temperatures 15, 25 and 35°C, an Arrhenius-type variation in the impact frequency is observed with a measured activation energy of  $18.9 \pm 0.4 \text{ kJ} \cdot \text{mol}^{-1}$ . If the impact frequency  $f$  is assumed to be dependent upon the rate of diffusional mass transport of the nano-material to the electrode surface, then, under a steady-state mass-transport regime,  $f$  should be proportional to the nanoparticulate diffusion coefficient. The diffusion coefficient of a given nanoparticle can be estimated on the basis of the Stokes-Einstein equation as given by  $D = k_B T / (6\pi\eta r_{np})$  where  $k_B$  is the Boltzman constant and  $r_{np}$  is the hydrodynamic nanoparticle radius. On the basis of this equation and the known viscosity of water as a function of temperature<sup>36</sup>, the activation energy for the diffusion of particulate material is predicted to be  $18.2 \text{ kJ} \cdot \text{mol}^{-1}$ . This value is in excellent agreement with the one found experimentally for the temperature range of 15-35°C, indicating that here the frequency of the nano-impacts events is determined by the rate of their mass-transport to the electrochemical interface. However, at 5°C the rate is significantly below that expected on the basis of the Arrhenius equation, indicating at this lower temperature a change in the rate-determining step. Consequently, the high sensitivity of the nano-impact experiment to the temperature is reflected in both the rate at which events occur and the rate of the electrochemical events themselves, stressing the importance of providing highly controlled thermostating of the system when studying such processes.

## Conclusions

Even for *model* thermostating systems, the temperature of the sample being thermostated can differ markedly from that of the bath (0.1-0.2 K as measured in the present work). Both evaporation and radiation can lead to significant cooling of the top layers of a solution. The resulting temperature gradient means that such systems tend to convective rather than quiescent stationary states. The volume-averaged flow velocities under such steady-state conditions can be not insignificant – simulations predict up to ca.  $10^{-4} \text{ m} \cdot \text{s}^{-1}$  for the present case ( $\sim 1 \times 10^{-4}$  and  $\sim 2 \times 10^{-4} \text{ m} \cdot \text{s}^{-1}$  for a closed and open cell, respectively). Note that the model described here does not include the mass transport in the cell – doing that would require solving a considerably more involved problem and thus exceed the aims of the current study. Nevertheless, it needs to be pointed out that the convective flows induced by temperature variations alone yield fluxes comparable in magnitude to the diffusive ones commonly encountered in the electrochemical systems.

The following design guidelines for thermostating may be outlined from these model experiment and simulations.

1. The temperature of the sample needs to be measured directly as it can differ significantly from that of the heated bath.
2. Evaporation must be avoided in all cases by using a closed system. This is true even when using large (ca. mL) quantities of solution.

3. The time necessary for a cell to approach a steady state is to a large extent controlled by the convective flows in the cell. The use of forced convection to ensure a homogeneous solution phase temperature is advisable.

These insights are specifically useful for the design of electrochemical systems. As demonstrated in this work, nanoelectrochemical reactions are highly sensitive to the local temperature – both the frequency and the rate of the oxidation of individual silver nanoparticles were shown to be temperature-sensitive.

More generally, the highlighted importance of heat transfer by evaporation and radiation in controlling the temperature of thermostated systems is of wide significance. It needs to be emphasized that as the amount of solution being thermostated decreases and the area of the liquid|air interface increases relative to the volume, the importance of evaporation in creating local temperature gradients can be expected to become ever more significant.

**Acknowledgements.** This project has received funding from the European Research Council (ERC) under the European Union's Horizon 2020 research and innovation programme (grant agreement No 727292). This project is supported by the funding from the European Research Council under the European Union's Seventh Framework Programme (FP/2007-2013)/ERC Grant Agreement no. [320403]. J.K.N. thanks the Clarendon Fund and Trinity College of the University of Oxford for a Clarendon-Titley scholarship.

## References

1. A. Einstein, *Ann. Phys. (Leipzig)*, 1905, **322**, 549-560.
2. W. Sutherland, *Phil. Mag.*, 1905, **9**, 781-785.
3. J. A. V. Butler, *Trans. Faraday Soc.*, 1924, **19**, 734-739.
4. J. A. V. Butler, *Trans. Faraday Soc.*, 1924, **19**, 729-733.
5. J. A. V. Butler, *Trans. Faraday Soc.*, 1924, **19**, 659-665.
6. A. J. Bard and L. R. Faulkner, *Electrochemical Methods: Fundamentals and Applications*, Wiley, 2000.
7. V. G. Levich, *Physicochemical Hydrodynamics*, Prentice-Hall, Inc., Englewood Cliffs, N.J., 1962.
8. J. K. Novev and R. G. Compton, *Curr. Opin. Electrochem.*, 2018, **7**, 118-129.
9. S. V. Sokolov, S. Eloul, E. Kätelhön, C. Batchelor-McAuley and R. G. Compton, *Phys. Chem. Chem. Phys.*, 2017, **19**, 28-43.
10. N. V. Rees, *Electrochem. Commun.*, 2014, **43**, 83-86.
11. M. Pumera, *ACS Nano*, 2014, **8**, 7555-7558.
12. W. Cheng and R. G. Compton, *TrAC, Trends Anal. Chem.*, 2014, **58**, 79-89.
13. Y.-G. Zhou, N. V. Rees and R. G. Compton, *Angew. Chem.*, 2011, **123**, 4305-4307.
14. E. J. E. Stuart, K. Tschulik, C. Batchelor-McAuley and R. G. Compton, *ACS Nano*, 2014, **8**, 7648-7654.
15. W. Cheng, X.-F. Zhou and R. G. Compton, *Angew. Chem. Int. Ed.*, 2013, **52**, 12980-12982.
16. X. Xiao and A. J. Bard, *J. Am. Chem. Soc.*, 2007, **129**, 9610-9612.



17. L. S. Y. Ly, C. Batchelor-McAuley, K. Tschulik, E. Kätelhön and R. G. Compton, *J. Phys. Chem. C*, 2014, **118**, 17756-17763.
18. Z. Guo, S. J. Percival and B. Zhang, *J. Am. Chem. Soc.*, 2014, **136**, 8879-8882.
19. A. J. Bard, H. Zhou and S. J. Kwon, *Isr. J. Chem.*, 2010, **50**, 267-276.
20. X. Li, C. Batchelor-McAuley, S. A. I. Whitby, K. Tschulik, L. Shao and R. G. Compton, *Angew. Chem. Int. Ed.*, 2016, **55**, 4296-4299.
21. E. N. Saw, M. Kratz and K. Tschulik, *Nano Res.*, 2017, **10**, 3680-3689.
22. D. A. Robinson, Y. Liu, M. A. Edwards, N. J. Vitti, S. M. Oja, B. Zhang and H. S. White, *J. Am. Chem. Soc.*, 2017, **139**, 16923-16931.
23. K. Ngamchuea, R. O. D. Clark, S. V. Sokolov, N. P. Young, C. Batchelor-McAuley and R. G. Compton, *Chem. Eur. J.*, 2017, **23**, 16085-16096.
24. P. Bergé and M. Dubois, *Contemp. Phys.*, 1984, **25**, 535-582.
25. A. Sheludko, *Adv. Colloid Interface Sci.*, 1967, **1**, 391-464.
26. C. Batchelor-McAuley, J. Ellison, K. Tschulik, P. L. Hurst, R. Boldt and R. G. Compton, *Analyst*, 2015, **140**, 5048-5054.
27. L. D. Landau and E. M. Lifshitz, *Fluid Mechanics*, Pergamon Press, Oxford, Second edn., 1987.
28. Y. Jaluria, in *Heat Transfer Handbook*, eds. A. Bejan and A. D. Kraus, John Wiley & Sons, Hoboken, New Jersey, 2003, ch. 7, pp. 525-571.
29. T. L. Bergman, A. S. Lavine, F. P. Incropera and D. P. Dewitt, *Fundamentals of Heat and Mass Transfer*, Wiley, Hoboken, N.J., 7th edn., 2011.
30. D. R. Lide, *CRC Handbook of Chemistry and Physics, Internet Version 2005*, CRC Press, Boca Raton, FL, 2005.
31. W. M. Lai, D. H. Rubin and E. Krempel, *Introduction to Continuum Mechanics*, Elsevier Science, Burlington, MA, 4th edn., 2009.
32. I. B. Ivanov and D. S. Dimitrov, *Colloid. Polym. Sci.*, 1974, **252**, 982-990.
33. J. R. Keller and T. L. Bergman, *J. Heat Transfer*, 1990, **112**, 363-369.
34. B. F. Wang, Z. H. Wan, Z. W. Guo, D. J. Ma and D. J. Sun, *J. Fluid Mech.*, 2014, **747**, 447-459.
35. A. Lemembre and J. P. Petit, *Int. J. Heat Mass Transfer*, 1998, **41**, 2437-2454.
36. L. Korson, W. Drost-Hansen and F. J. Millero, *J. Phys. Chem.*, 1969, **73**, 34-39.